

Improvement of 20 in. diameter photomultiplier tubes

A. Suzuki and M. Mori

National Laboratory for High Energy Physics (KEK), Tsukuba, Ibaraki 305, Japan

K. Kaneyuki and T. Tanimori

Department of Physics, Tokyo Institute of Technology, Meguro, Tokyo 152, Japan

J. Takeuchi, H. Kyushima and Y. Ohashi

Hamamatsu Photonics K.K., Hamamatsu, Shizuoka 435, Japan

Received 24 July 1992 and in revised form 13 November 1992

The quality of the 20 in. photomultiplier tubes (Hamamatsu R1449) has been greatly improved over the required specifications for using them in the 50000 ton imaging water Cherenkov detector, Super-Kamiokande. In particular, the resolution of the timing response for single-photoelectron light has been reduced to ~ 3 ns (1σ width), and a clear single-photoelectron peak can be seen in the pulse height distribution. The obtained characteristics of the new tubes will make it possible to upgrade the performance of the Super-Kamiokande detector. The goal of the improvement, the procedure for designing the new tubes and the measuring results concerning the characteristics are described in detail.

1. Introduction

The 20 in. diameter photomultiplier tube (PMT) was originally developed for Kamiokande (Kamioka nucleon decay experiment) by Hamamatsu Photonics K.K. in cooperation with members of Kamiokande [1]. The Kamiokande detector is an imaging-type water Cherenkov detector with a total 3000 metric tons of water located 1000 m underground in the Kamioka mine [2]. A schematic of the cylindrical shape detector structure is depicted in fig. 1. A large photosensitive coverage of 20% of the detector inner surface equipped with 948 20 in. PMTs (see fig. 2) led to important experimental observations at Kamiokande. The detection of a neutrino burst from the supernova SN1987 A [3] and the observation of solar neutrinos while identifying the direction and measuring the energy of neutrinos [4] are pioneering events in neutrino astronomy. Under increasing demand upon experiments with large-size high-quality detectors, a 50000 ton water Cherenkov detector named Super-Kamiokande was proposed [5]. To realize the detector performance expected in Super-Kamiokande it is necessary to improve the quality of the present used 20 in. PMTs. In particular, a good timing response and a good energy resolution are essential factors, since they provide the necessary capabilities to determine the kinematical quanti-

ties of interaction events more accurately and to eliminate low-energy background events more efficiently. After about five years of R&D, we have developed high-quality 20 in. PMTs which satisfy the required characteristics of Super-Kamiokande.

2. Goal of improvement

The characteristics of the presently used 20 in. PMTs are discussed in detail in ref. [1]. The eight year running of Kamiokande to date has proved that the 20 in. PMTs were furnished with appropriate characteristics for use in a large-volume water Cherenkov detector. The detector has been running with stable operations, as shown in fig. 3, where the gain variation of this tube is shown to have been within $\pm 3\%$ over a period of four years. Our experiences in the Kamiokande experiment suggest that the improvement should polish individual quality of the tubes, since the fundamental design of the 20 in. PMT is almost satisfactory.

One of the main aims of the physics carried out at Super-Kamiokande is to detect low-energy neutrinos with high accuracy. A good timing response of the PMTs used in a water Cherenkov detector is a key factor since it allows a precise determination of the

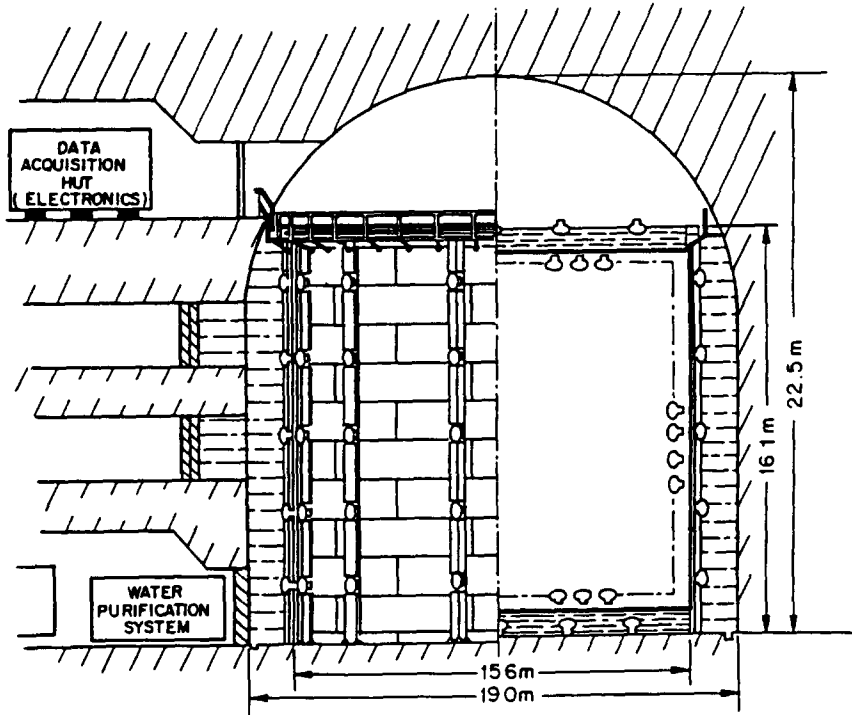


Fig. 1. 3000 ton Kamiokande water Cherenkov detector. The inner detector viewed by 948 20 in. PMTs is surrounded by a 4π water Cherenkov anticounter, also viewed by 123 20 in. PMTs.

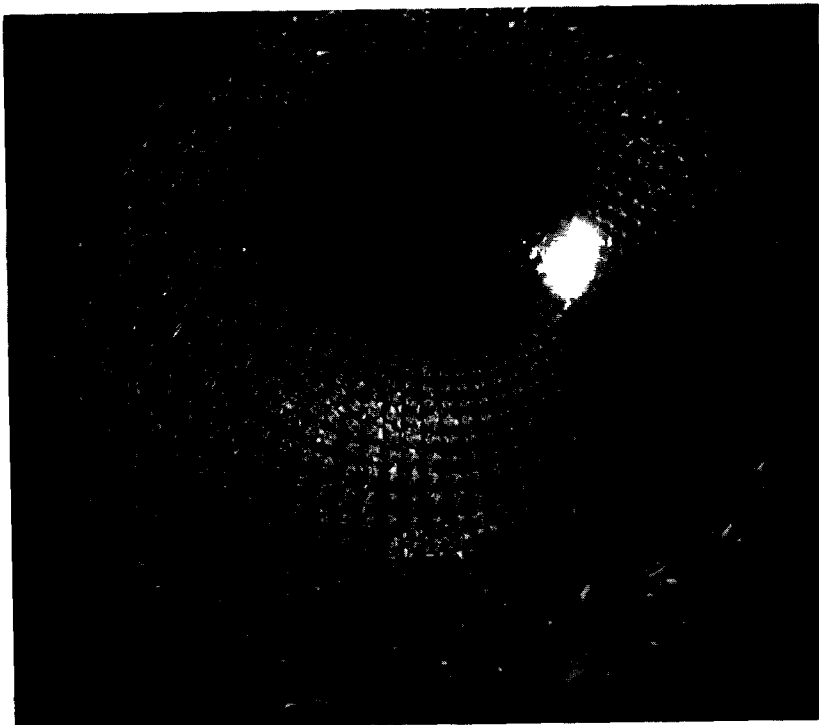


Fig. 2. The inside view of the Kamiokande detector. The 20 in. PMTs are uniformly placed facing inward on a 1 m grid on the entire inner surface. This picture was taken by a wide-angle lens, being viewed from the bottom.

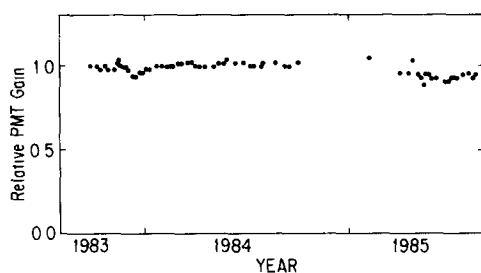


Fig. 3. Drift of average PMT gain in Kamiokande

event vertex point and direction of emitted Cherenkov light. In order to improve the resolution of the vertex point determination down to 50 cm for 10 MeV electrons, less than a 3 ns ($1 \text{ ns} = 10^{-9} \text{ s}$) time resolution (1 standard deviation) for single-photoelectron light is necessary. From the time resolution of typical present 20 in. PMTs (fig. 4) a factor of ~ 1.5 improvement is required for the new PMTs.

In neutrino interactions with the energy $< 10 \text{ MeV}$, the Cherenkov light received by each PMT in Super-Kamiokande is almost at a single-photoelectron level. Therefore, an improvement in the energy resolution in detecting these neutrinos requires an identification of the single-photoelectron peak in the PMT pulse height distribution. In the presently used PMTs, no clear single-photoelectron peak is found, as shown in fig. 5. In addition to providing accurate detection of low-energy neutrino events, the good timing and energy resolution of the PMTs provide an efficient elimination of background events (γ - and β -rays) produced from the decay of ^{238}U , ^{232}Th , ^{226}Ra , ^{222}Rn and ^{40}K contaminated in the detector materials. This is because the lower energy resolution causes a misidentification of the energies of γ - and β -rays as being more energetic; the wider space resolution of the vertex point causes a misidentification of background events coming from outside the detector as contained events. In order to realize a threshold energy less than 5 MeV in Super-

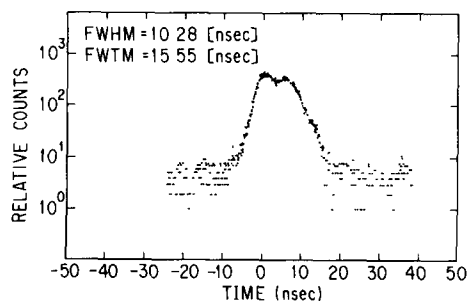


Fig. 4. Single-photoelectron transit time distribution of the present 20 in. PMT.

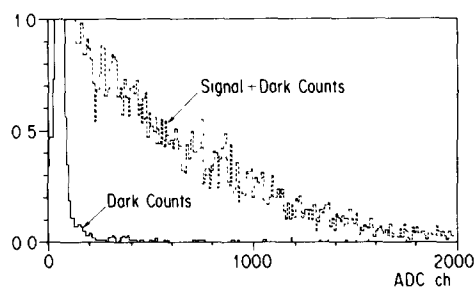


Fig. 5. Single-photoelectron pulse height distribution of the present 20 in. PMT.

Kamiokande, PMTs with good energy and timing resolutions are requisite.

In Super-Kamiokande, which uses 11200 20 in. PMTs, the event trigger rate induced from the random coincidence of PMT dark pulse counts cannot be ignored. The random trigger rates expected in Super-Kamiokande for trigger threshold energies of 5 and 7 MeV are listed in table 1 as a function of the PMT dark count rate, where the dark count rate is defined by the rate of pulses greater than $1/4$ photoelectron in magnitude. To maintain the 5 MeV threshold energy of event trigger, dark count rate of less than $3 \sim 4 \text{ kHz}$ for each PMT is demanded. Fortunately, at a temperature of 10°C in the Kamiokande detector water, the dark count rate of most of the present 20 in. PMTs has been found to be less than 3 kHz. Hence, the goal of this parameter is not so tight.

A large-diameter photomultiplier is critically sensitive to the geomagnetic field. Our plan is to use 20 in. PMTs without a magnetic shield material (like permalloy or a high- μ material). In Super-Kamiokande the residual amplitude of the geomagnetic field inside the detector would be suppressed to less than 100 mG by using compensating current coils around the detector. Thus, it is required that the new PMTs should preserve their characteristics under zero magnetic field up to under 100 mG.

Table 1
Expected random trigger rate vs PMT dark count rate in Super-Kamiokande

Dark count rate [kHz]	Trigger threshold energy	
	$E_{\text{th}} = 5 \text{ MeV}$	$E_{\text{th}} = 7 \text{ MeV}$
2	4.6×10^{-6}	1.2×10^{-15}
3	2.3×10^{-2}	3.5×10^{-10}
5	2.3×10^2	8.1×10^{-4}
6	—	9.3×10^{-3}
7	—	3.5
10	—	6.9×10^3

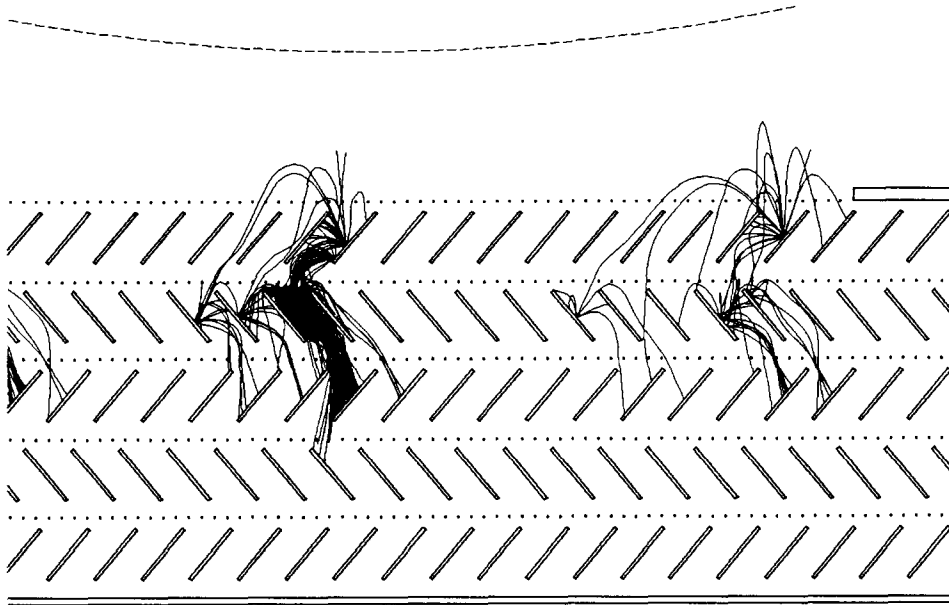


Fig. 6. Electron trajectories simulated for the present 20 in. PMT dynode.

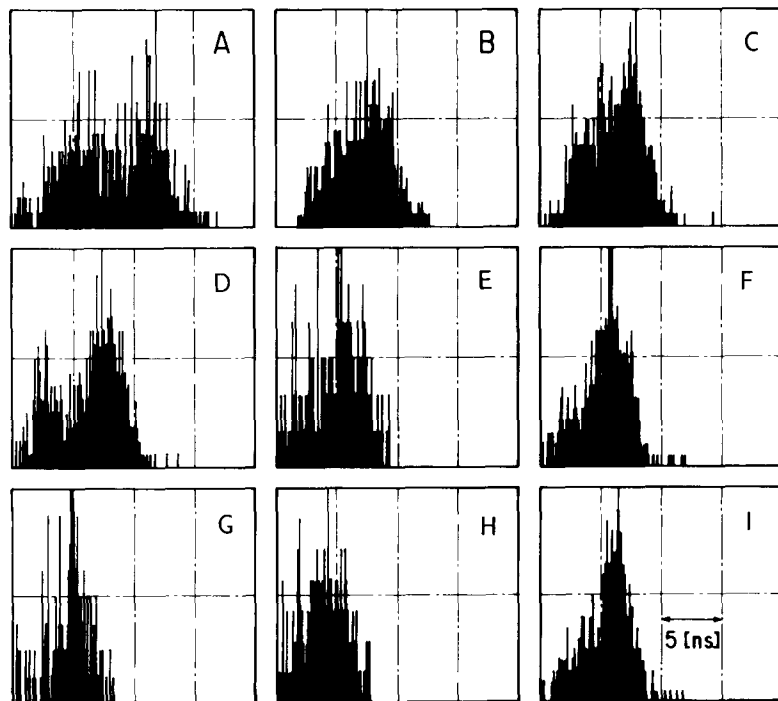


Fig. 7. Simulated single-photoelectron transit time distributions for the present 20 in. PMT(A) and the proposed dynode structures (B ~ I). One division in the figure corresponds to 5 ns.

3. How to design high-quality 20 in. PMTs

It is not too much to say that the PMT characteristics are determined mainly by the dynode structure. A venetian blind type dynode is a unique solution for the 20 in. PMT in terms of its large photosensitive area. However, among various types of dynode structures, a venetian blind type results in a rather smaller collection efficiency for electrons. This causes the timing response and energy resolution to become worse. Therefore, to understand how the primary and secondary electron collection efficiency is increased is essential regarding this improvement. Utilizing a Monte Carlo technique to simulate secondary electron trajectories from one dynode to the next, provides a visual approach to understand the effects of the dynode structure parameters on electron trajectories. Fig. 6 shows simulated secondary electron trajectories, using the dynode parameters of the present 20 in. PMT. In this figure one can see that there are some trajectories which hit the same dynode plate again and the neighbouring plate in the same stage, some trajectories pass through the gap of the plates without hitting, and some have long flight paths. Reducing these abnormal trajectories results in improving better PMT properties. By applying this visual method we tried to optimize all of the parameters which characterize the dynode struc-

ture, so as to achieve good timing and energy resolutions. Typical parameters of dynode structure are the shape, length and slope of the plate; the gap between plates in the same stage; the distance and relative position of one dynode to the next dynode stage; the ratio of voltage division, and so on.

Figs. 7 and 8 show Monte Carlo simulation results for the single-photoelectron time response presented by a transit time and the single-photoelectron pulse height distribution for the present 20 in. PMT (A) and for proposed venetian blind dynode structures with different parameter values (B ~ I). Here, the simulation of electron trajectories is followed up from the first to the third dynode stage, because the PMT qualities are almost characterized by the earlier stages, and the other backward stages contribute only to statistical fluctuation. The transit time simulation of the present PMT (fig. 7a) shows a two-bump shape and 10 ns FWHM (full width at half maximum). Both results agree quite well with the observed data shown in fig. 4. As for the energy response, the simulation result for the present PMT (fig. 8a) shows no clear peak, being unseparated from the signals of abnormal trajectories which peak at the lower side of the distribution. This also agrees with the observed single-photoelectron pulse height distribution shown in fig. 5. Such a good correspondence between the observation and simula-

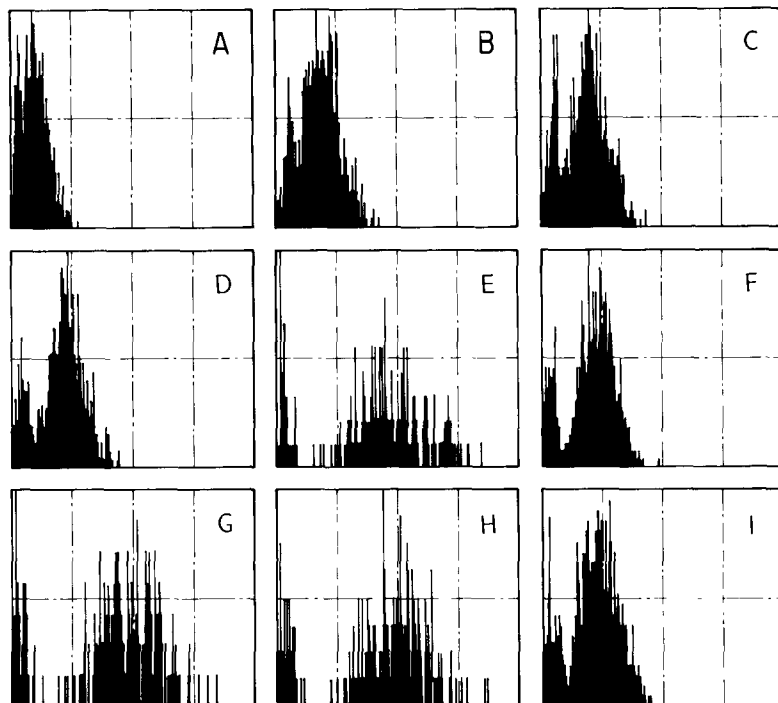


Fig. 8. Simulated single-photoelectron pulse height distributions for the present 20 in. PMT(A) and the proposed dynode structures (B ~ I).

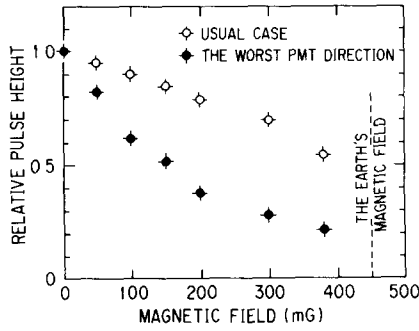


Fig. 9. Effect of an external magnetic field for the present 20 in. PMT.

tion implies that the Monte Carlo method is practical for the purpose of designing the dynode structure of PMT. Among the proposed dynode structures (B ~ I), types (F ~ I) give a narrow transit time spread of (5~7) ns (FWHM) and a clear single-photoelectron peak. These dynode types could provide sufficient characteristics to satisfy the goal values of this improvement.

Photoelectrons traversing from the cathode surface to the first dynode are deflected by Earth's geomagnetic field; therefore, some of them fail to hit the first dynode. Fig. 9 shows the change of the anode pulse height due to an external magnetic field for the present 20 in. PMT. About a factor 10 reduction of the output pulse-height is observed at a field of 400 mG for the worst case. The simplest way to overcome one of the influences of a magnetic field is to enlarge the dynode size. Figs. 10a and 10b are maps of photoelectron hitting points on the first dynode plane in a 100 mG magnetic field for two different field directions, parallel (fig. 10a) and perpendicular (fig. 10b) to the dynode

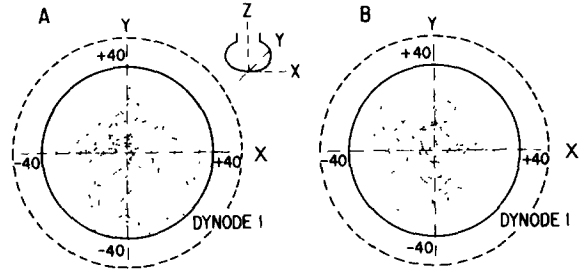


Fig. 10. Photoelectron hit points on the first dynode plane in a 100 mG magnetic field applied in parallel (a) and perpendicular (b) directions to the blind plane. (Units in mm.)

plate. The size of 38 mm radius of the present PMT (solid circles) causes the loss of some hits; the proposed 48 mm dynode radius (dashed circles) for the new 20 in. PMT, however, saves all hit points.

Various types of dynode structures were proposed based on the simulation results. By interplaying among the simulation, trial constructions and quality measurements we could determine the final dynode structure for the new 20 in. PMT.

4. Characteristics of new 20 in. PMT

4.1. Fundamental design

The size and shape of the new 20 in. PMT are almost the same as that of the old ones. A minor modification to lengthen the glass multisealing line near the socket (see fig. 11) was made. This makes the waterproof structure attach to the glass more tightly. The photocathode material is of bialkali (Sb-K-Cs)

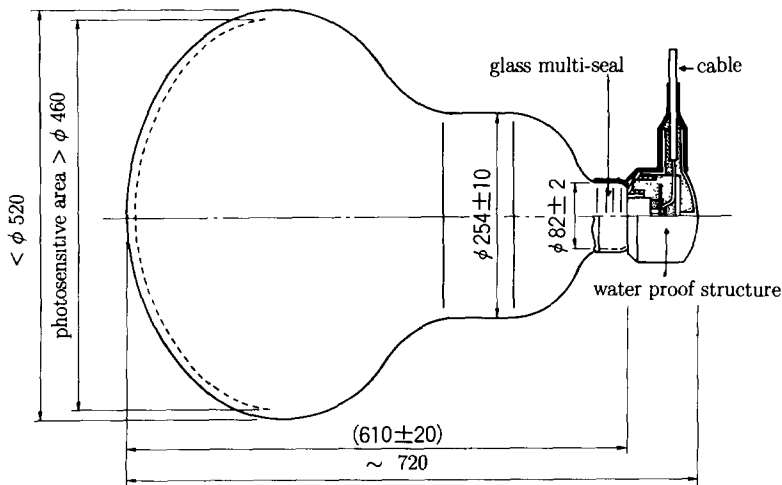


Fig. 11. Schematic of the new 20 in. PMT (units in mm).

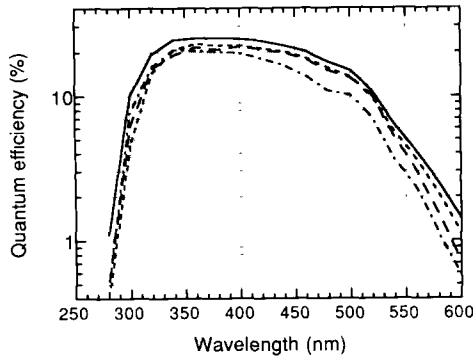


Fig. 12. Quantum efficiency.

owing to its high spectral sensitivity for blue light and its low thermionic emission. The spectra response of the photocathode is determined by both the photocathode material and the light transmission efficiency of glass window. The quantum efficiency (QE) is plotted in fig. 12 as a function of the wavelength of input light. The average value of QE at $\lambda = 390 \text{ nm}$ ($1 \text{ nm} = 10^{-9} \text{ m}$) is equal to 22%. The dynode structure (venetian blind type) was drastically changed. The bleeder chain illustrated in fig. 13 was optimized with an 11-stage voltage divider (8-3-1-...-1), while also adding three types of focusing mesh plates between the cathode and the first dynode.

4.2. Gain

The PMT gain is defined by the ratio of the anode current to the photocathode current. Diffused light

from tungsten lamp at color temperature 2856 K is used for this measurement. Fig. 14 shows the gain vs supplied voltage curve. It is obvious that the gain increases linearly in the log-log scale as the voltage up to 2500 V. The values of supplied voltage which gives a gain of 10^7 are distributed around 2000 V, as shown in fig. 15; this is nearly the same as those of the old tubes. Quality measurements of the new tubes presented in the following were carried out at this 10^7 gain when no stated differently.

4.3. Timing response

An accurate timing response is one of the most interesting characteristics of the 20 in. PMT, due to its large photosensitive area. The transit time (TT), anode pulse waveform and transit time spread (TTS) were measured. TT was measured by comparing the response time difference between the new tubes and a 3/8 in. tube, illuminating 410 nm diffused light from a fast laser pulser with ps rise time (Hamamatsu PLP-01), where the TT of a 3/8 in. tube is 8.65 ns measured separately by comparing it with the response of PIN photodiode. The average TT value is about 100 ns for multiphotoelectron light. The same method to obtain single-photoelectron light is used in the following quality measurements of the new tubes. TT is a function of the supplied voltage as shown in fig. 16, where the TT values of several PMTs are plotted. About a 10 ns variation of TT is seen, corresponding to a supplied voltage range of 1500 to 2500 V. Such timing difference of each PMT is calibrated in Super-Kamiokande by making use of a laser diffuser hanging at the center of the detector (see ref. [2]).

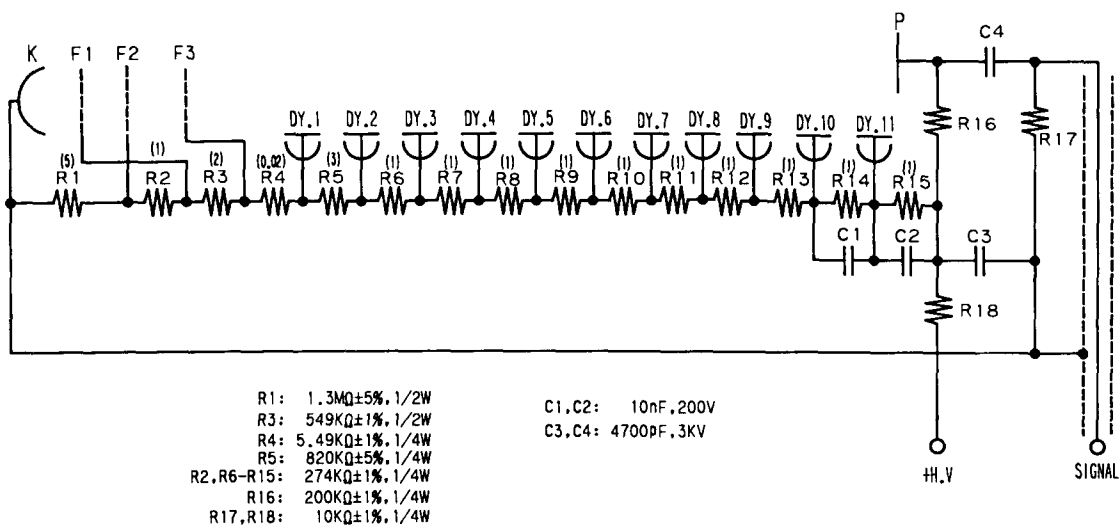


Fig. 13. Bleeder chain.

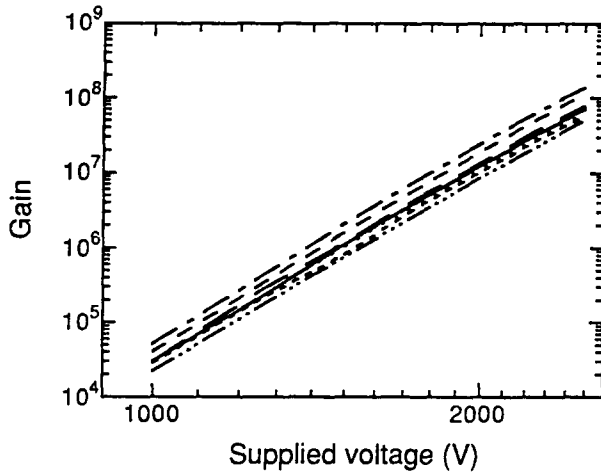


Fig. 14. Gain vs supplied voltage.

The anode pulse waveform for δ -function shaped input light (410 nm) of ~ 10 photoelectrons was measured. The rise and fall times are nearly 10 ns, and the anode pulse width (FWHM) is about 18 ns. The timing response is greatly improved, compared with the ~ 20 ns rise time, ~ 50 ns fall time and ~ 30 ns FWHM of the old tubes. According to the Monte Carlo simulation, such a good timing response is a result of the high collection efficiency of secondary electrons which, moreover, move through shorter flight paths between dynodes. The supply voltage dependence of the rise and fall times is given in fig. 17.

Timing measurements in the experiments is generally limited by the variation of TT in each light pulsing due to the different initial velocities and initial directions of photoelectrons emitted from the photocathode, the different electric fields between the cathode and the first dynode, and between the dynodes resulting from the electrode geometry. TTS represents the jitter of TT and, hence, provides the time resolution of

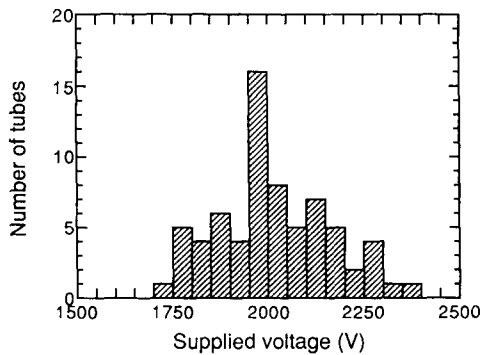


Fig. 15. Distribution of supplied voltage providing 10^7 gain.

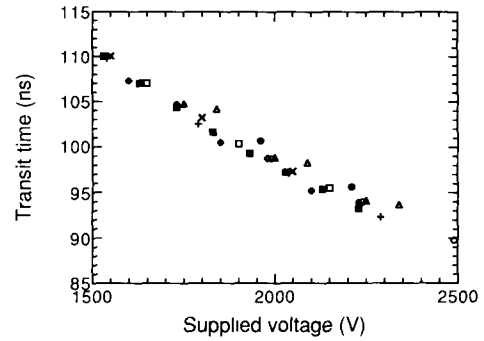


Fig. 16. Transit time vs supplied voltage.

PMT. The block diagram of photon counting used in the present measurements is depicted in fig. 18. Here, single-photoelectron light is identified by observing a single-photoelectron peak of 2 in. tube as shown in fig. 19. The fractions of signal count rate to the laser pulser frequency are 7% for fig. 19a and 21% for fig. 19b. Based on Poisson statistics, above 96% of the input light in the measurement of fig. 19a is single-photoelectron equivalent. In the case of fig. 19b it is expected that the single-photoelectron component in the input light is 88% and the two-photoelectron component is 12%. Therefore, the lower peak in fig. 19 corresponds to single-photoelectron light and the higher peak to two-photoelectron light. A typical relative TT distribution taken by fully diffused illumination of single-photoelectron light with 410 nm wavelength is shown in fig. 20. One can see the narrow width peak, which is different from the two-bump shape seen in the old tube. 2.2 ns (1σ) for TTS is obtained by fitting this distribution to an asymmetric Gaussian shape function. The TTS values for ten new tubes are distributed within $\sigma \sim 3$ ns, as shown in fig. 21. This result is satisfactory for using new tubes in Super-Kamiokande.

The photocathode position dependence of TT is measured using the scheme shown in fig. 22, where the

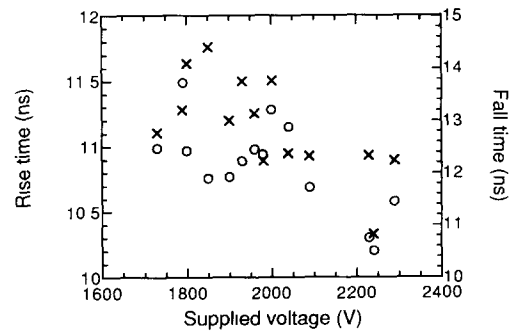


Fig. 17. Rise time (O) and fall time (X) vs supplied voltage.

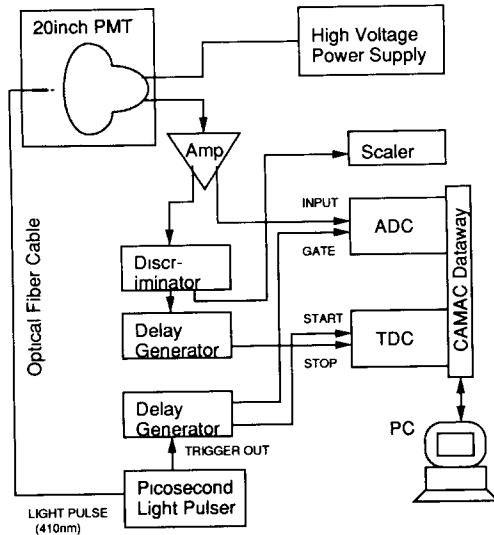


Fig. 18. Block diagram of photon counting measurement.

light position is represented by θ , the angle between the incident optical axis and the PMT axis (Y-direction). Measurements were carried out by moving a light with a spot shape along two different directions: perpendicular to the dynode plane (Y-direction) and parallel to it (X-direction). The results of relative TT are shown in fig. 23. One can find no significant change of TT over nearly the entire photosensitive area.

4.4. Pulse height distribution

The most significant effort made in the present improvement was to be able to identify the single-pho-

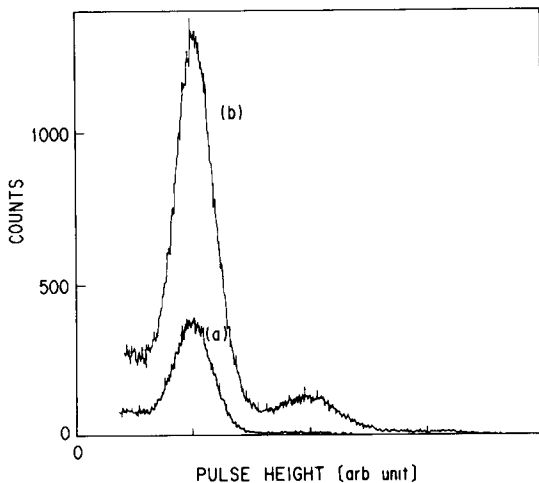


Fig. 19. Pulse height distributions of 2 in. tube. Ratios of the signal count rate to 410 nm light frequency from a fast laser pulser are 7% for (a) and 21% for (b).

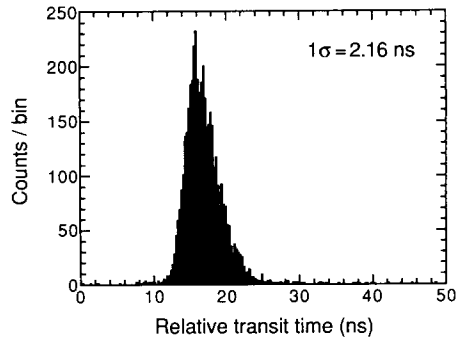


Fig. 20. Relative transit time distribution.

toelectron peak, being well separated from the dark noise distribution. Fig. 24 shows the pulse height distribution of the single-photoelectron input, measured using full diffused blue light (410 nm) (see block diagram of fig. 18). A clear peak can be seen around the 400 channel of ADC counts. Here, the noise distribution causes a spike shape near the lowest ADC channel. The result of fig. 24 is impressive, compared with the data of the old tube (see fig. 5). The peak-to-valley ratio (P/V), which is defined as being the peak height of the distribution divided by the minimum value between the signal peak and the noise peak, signifies the kurtosis of the peak. P/V is observed to be 1.9 on the average from the P/V plots of several tubes in fig. 25.

The uniformity of the pulse height distribution is measured using the same scheme as that of TT; the results are shown in fig. 26. Clear peaks can be also observed over the entire photosensitive area. Different pulse height distributions observed in fig. 26 come from the anode nonuniformity discussed below. The P/V ratios derived from fig. 26 are plotted as a function of θ in fig. 27. Such well-separated pulse height distributions for single-photoelectron light makes it possible to take data for low-energy neutrino events (energy ≤ 10 MeV) with good energy resolution.

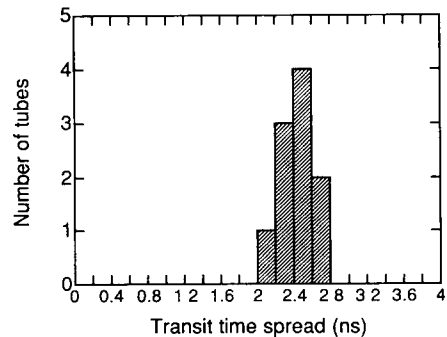


Fig. 21. Transit time spread (1σ width) distribution.

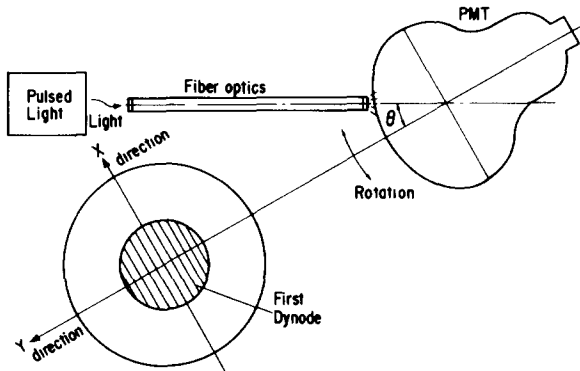


Fig. 22. Layout of a uniformity measurement.

4.5. Collection efficiency

The collection efficiency was measured by comparing the counting rate of the 20 in. PMT with that of the 2 in. PMT, illuminating single-photoelectron diffused blue light with a spot size of 20 mm ϕ . The collection efficiency of the 2 in. tube was obtained to be 90.3%, making use of the same spot light as the present case and comparing the signal count rate with the cathode current. The 20 in. photon counting was taken by setting the pulse discrimination level at the valley point of the single-photoelectron pulse height distribution and by setting a 50 ns timing window for the transit time. The average value of the absolute collection efficiency for new tubes was 70%, which is larger by a factor of ~ 1.5 than that of a standard venetian blind dynode (40–50%). Such high collection efficiency results in a good timing response and good energy response of the new tubes. The photocathode position dependence of the collection efficiency is shown in fig. 28. The distribution is quite uniform within a difference of $\pm 7\%$.

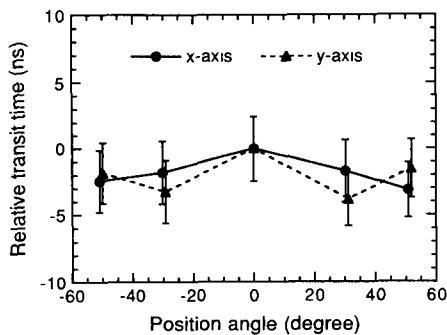


Fig. 23. Uniformity of relative transit time. Error bars indicate TTS.

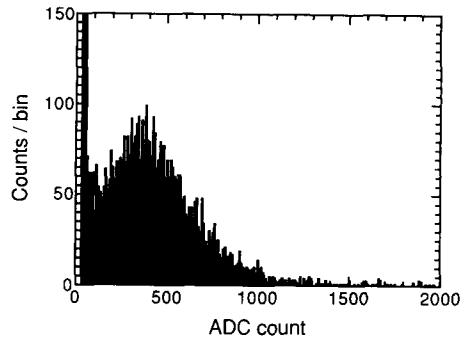


Fig. 24. Single-photoelectron pulse height distribution for full diffused illumination.

4.6. Cathode and anode uniformities

The cathode nonuniformity directly reflects the nonuniformity of the quantum efficiency. The cathode current was measured, by applying a +150 V between the cathode and the first dynode, and making use of a tungsten lamp. The results of spot illumination on different photosensitive positions are compared and plotted in fig. 29. The definition of the position is the same as that given in fig. 22. The uniformities of the X- and Y-directions were obtained to be $\pm 5\%$ and $\pm 10\%$, respectively. Evaporation of alkali metal onto the photocathode is very uniform for this large dimension.

The anode uniformity depends mainly upon the uniformity of the collection efficiency of each dynode stage. Fig. 30 shows the anode current variation as a function of θ , where the data are normalized at $\theta = 0$ for each PMT. The observed nonuniformity is within $\pm 40\%$ for the X- and Y-directions.

4.7. Dark current, dark count and afterpulse

Main noise sources at a gain high voltage of 10^7 are considered as being the thermoionic emissions of elec-

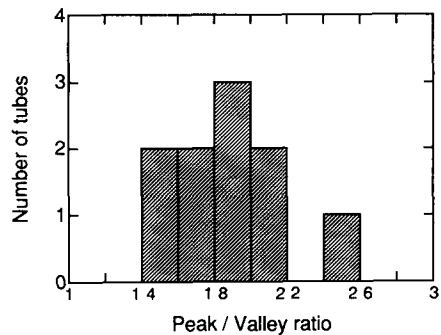


Fig. 25. Peak-to-valley ratio for single-photoelectron light.

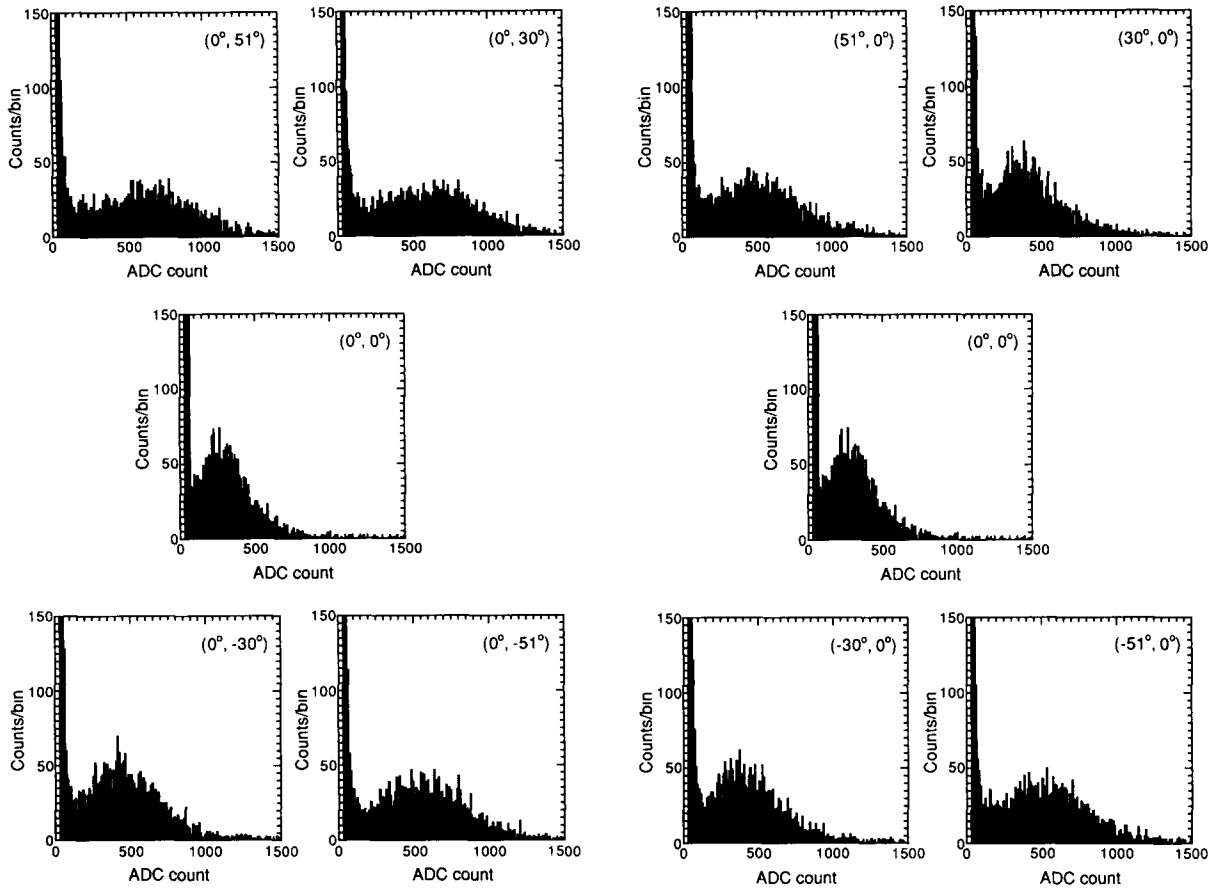


Fig. 26. Photocathode position dependence of the single-photoelectron pulse-height distribution, where $(0^\circ, 51^\circ)$ means that the light-illuminating point is at 0° along the X-axis and 51° along the Y-axis.

trons from the photocathode and the dynodes, as well as ohmic leakage due to the imperfect insulation of the dynode-supporting materials. Particularly, since the dynode-to-dynode distance for new tube is shorter by 1/2 compared to the old one, the noise due to imperfect insulation is serious. The observed dark currents are distributed within 200 nA, as shown in fig. 31.

Since the dark noise pulse spectrum dominates for a low pulse height, as can be seen in the single-photoelectron pulse height distribution (fig. 24), most of the dark noise scarcely influence the experiment in the case that the threshold level for each PMT is set at the valley point. The distribution of the dark count rate, which was measured by counting the dark pulses with

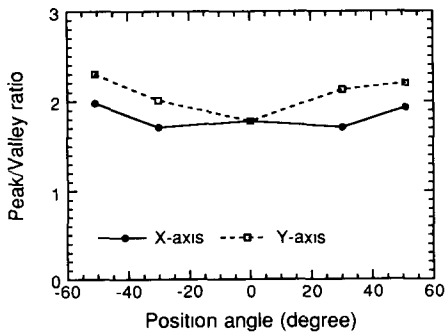


Fig. 27. Uniformity of P/V ratio.

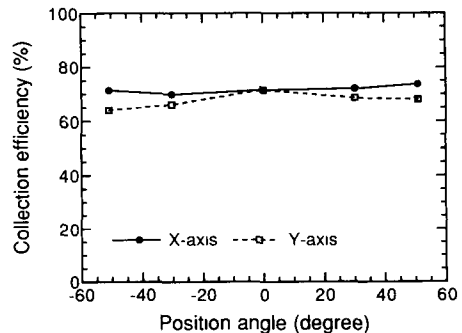


Fig. 28. Uniformity of the collection efficiency.

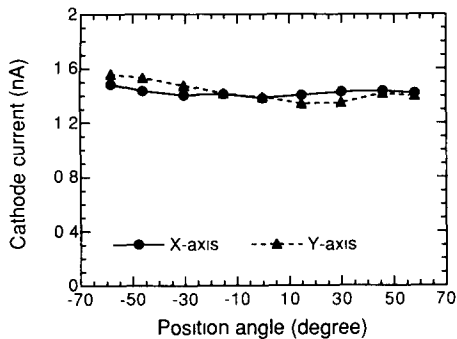


Fig. 29. Cathode uniformity.

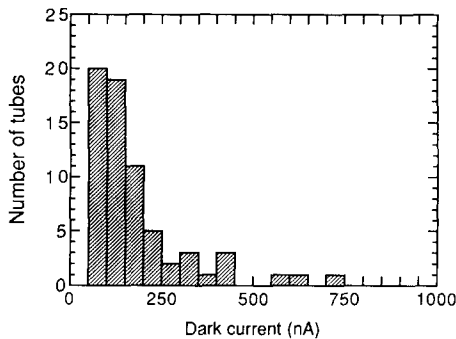


Fig. 31. Dark current distribution.

their pulse height larger than 1/6 photoelectron, is shown in fig. 32. The average value is 20 kHz, which is somewhat higher than the goal value of 3 kHz discussed in section 2. However, it is noted that the observed dark count rate for the 20 in. photosensitive area is relatively small as compared with ~ 500 Hz of typical 2 in. tubes. According to previous experience involving the mass production of the 20 in. PMT, the dark count rate would be reduced as production increases.

Temperature is one of the factors which can reduce the dark noise rate. Fig. 33 shows the temperature dependence of the dark count. From this figure we can expect a factor of 4 reduction when the PMTs are

used in 10°C water. It is our plan to keep the detector water temperature at 10°C in Super-Kamiokande.

Afterpulsing over a long time interval (up to tens of ms) was examined. A sizeable pulse was observed as a broad shape over a time range of ~ 10 μs after an ~ μs time delay of the main pulse. The amplitude of afterpulse was found to be ~ 0.4% of the input pulse.

4.8 Magnetic properties

All of the properties described above were measured under the condition of zero magnetic field after compensating for the Earth's geomagnetic field using a high μ-metal box. In Super-Kamiokande the geomagnetic field can be decreased down to less than 100 mG with the aid of a current network system around the water tank. Thus, 20 in. PMTs are required to preserve the qualities in the presence of a 100 mG external magnetic field. To observe the sensitivity to a magnetic field, the timing and pulse height responses for illuminating single-photoelectron diffused light were measured by applying a static magnetic field generated by double (vertical and horizontal) Helmholtz coils.

TT relative to that of no magnetic field and TTS are plotted in figs. 34a and 34b, for the case that the magnetic field was applied in the range of -500 to 500

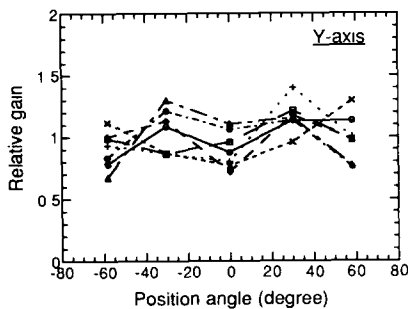
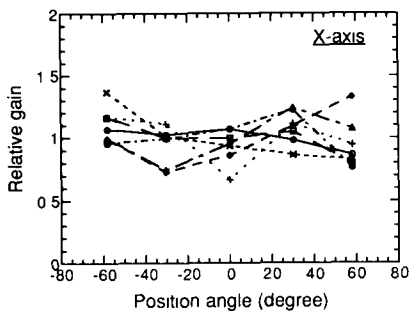


Fig. 30. Anode uniformity.

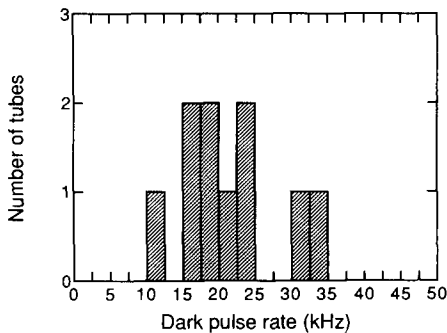


Fig. 32. Distribution of dark pulse rate.

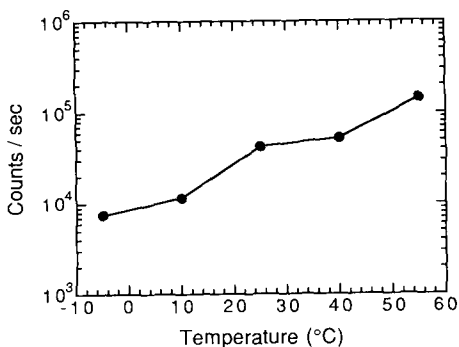


Fig. 33. Dark pulse rate as a function of temperature.

mG, parallel, respectively to the X-, Y-, and Z-axis. The definition of the axis is the same as that in fig. 22. One can see that the variation of the timing response is negligibly small within ± 500 mG external field. Under the same measuring condition the counting rate and the pulse height distribution were measured. Fig. 35a shows the relative counting rate, taken with a fixed discrimination level of 0.15 photoelectron and a fixed timing interval between ± 25 ns around the center of the transit time. Upon applying a 100 mG magnetic field to the X- and Y-axis, about a 10% reduction was observed. Considering the total size of the dynode plates of the new tubes (see fig. 10), this reduction might come from the increment of photoelectrons passing through the gap between the first dynode blinds without hitting. The integrated pulse height above the discriminator level is plotted in fig. 35b. The variation is similar to that of the count rate.

The measurements were also carried out for the worst reduction case of the sensitivity to the magnetic field, where a light source with a spot shape is set at two different positions apart from the center of the photocathode by 60° along the X- and Y-axis. These

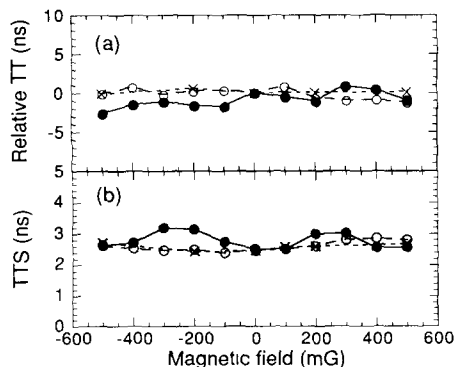


Fig. 34. Relative transit time (a) and TTS (b) vs external magnetic field. \bullet stands for the field parallel to X-axis, \circ to Y-axis and \times to Z-axis.

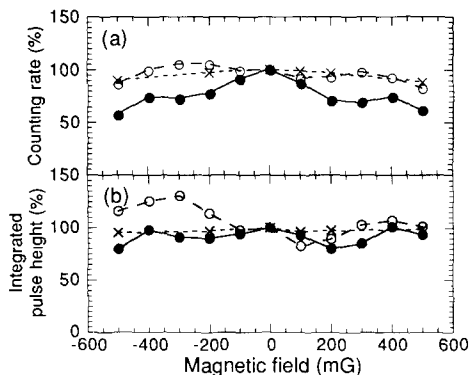


Fig. 35. Counting rate (a) and integrated pulse height (b) vs the external magnetic field. The data points are normalized at zero magnetic field. The symbols have the same definitions as in fig. 34.

positions are almost the edge of the photocathode surface, as can be seen in fig. 22. The observed results concerning the relative TT and TTS are plotted in fig. 36. At most a 2 ns change of TT is observed at 100 mG. Since the TT of each tube is calibrated by laser light, this change has no effect on the experiment. Experimentally, TTS is essential. Fig. 36 shows that new tubes

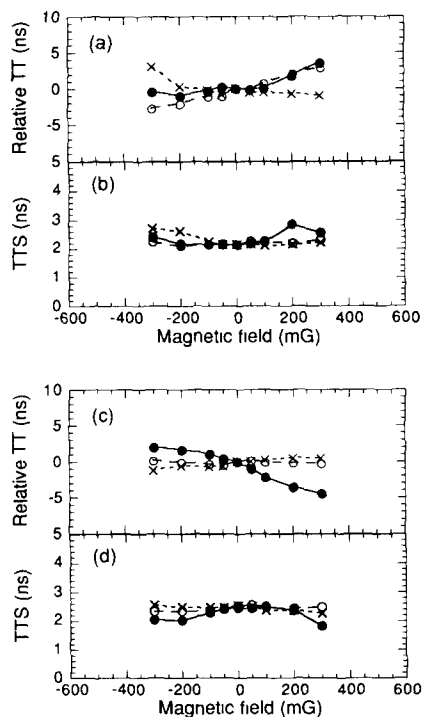


Fig. 36. Relative TT and TTS at the light positions of 60° along the X-axis ((a) and (b)) and along the Y-axis ((c) and (d)). The symbols have the same definitions as in fig. 34.

have no significant change of TTS within 100 mG, even under this severe condition. Fig. 37 gives the count rate and integrated pulse height for two light positions. One can see about a 25% change in the count rate and about a 50% change in the integrated pulse height at 100 mG as the worst value. From an energy resolution point of view in the experiment, the change in the count rate is essential for single-photoelectron light. This 25% difference is within the range of compensation in Super-Kamiokande, since there are a number of hit-PMTs in one Cherenkov ring: for instance, ~ 50 hit-PMTs for 10 MeV electrons.

4.9. Waterproof structure

The new 20 in. PMTs are installed at a maximum water depth of 42.5 m in Super-Kamiokande. Tight waterproofing around the bleeder chain board and the cable extraction is thus requisite. A schematic view of the waterproof structure is depicted in fig. 38. Two kinds of polyethylene frames stand on the neck bottom of the PMT glass bulb. These frames are wrapped by two polyethylene heat shrinking tubes: one covers over both the frame and the glass; the other contacts both on the frame nose and the cable. Water pressurizing tests have been continuing. So far, the proposed water-

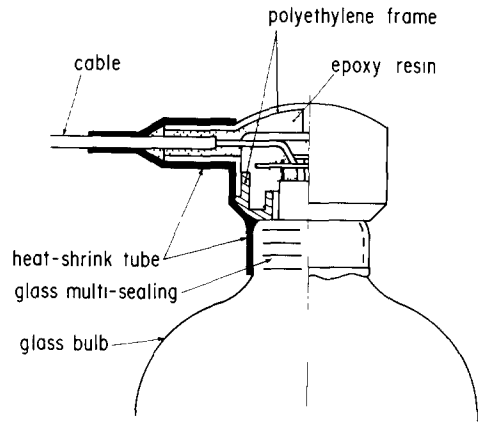


Fig. 38. Waterproof structure of the new 20 in. PMT.

proof structure has been proved to be sufficient for use up to a water depth of 70 m. Above this water pressure, some of the tested tubes (about 10%) showed cracks at the glass multisealing part (see fig. 38).

5. Conclusion

The major qualities of 20 in. PMTs have been drastically improved. Among them an improvement of the timing response (transit time spread) and energy response (pulse height distribution) for single-photoelectron light makes it possible to carry out low-energy (< 10 MeV) neutrino measurements with high accuracy at Super-Kamiokande.

Acknowledgement

We are most grateful to M. Koshiba and Y. Totsuka for their encouragement and suggestion. We are very grateful to the people of Hamamatsu Photonics K.K. and Kamiokande for useful discussions, and to the people of Fujikura Ltd. for the design of waterproof structure. We also wish to thank H. Sugawara, K. Takahashi, S. Iwata, T. Nishikawa and J. Arafune for their encouragement and support. Some parts of this work were supported by a Grant-in-Aid for Developmental Scientific Research from the Ministry of Education, Science and Culture under contract no. 61840003 and 02554005.

References

- [1] H. Kume et al., Nucl. Instr. and Meth. 205 (1986) 443.
- [2] K.S. Hirata et al., Phys. Rev. D38 (1988) 448; and Phys. Rev. D44 (1991) 2241.

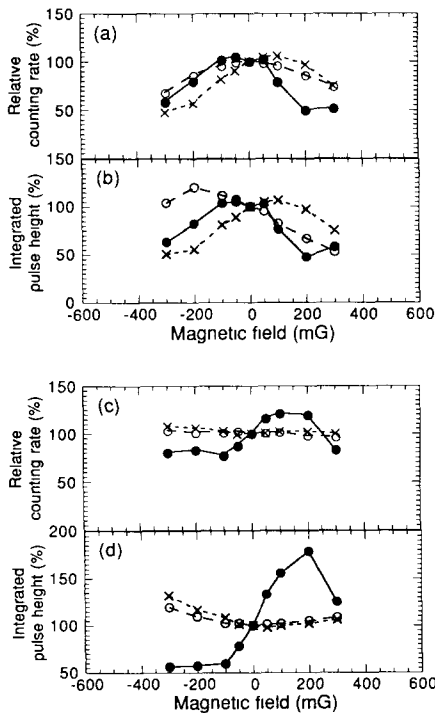


Fig. 37. Relative count rate and integrated pulse height at the light positions of 60° along the X-axis ((a) and (b)), and along the Y-axis ((c) and (d)). The symbols have the same definitions as in fig. 34.

- [3] K.S. Hirata et al., Phys. Rev. Lett. 58 (1987) 1490.
- [4] K.S. Hirata et al., Phys. Rev. Lett. 63 (1989) 16; Phys. Rev. Lett. 65 (1990) 1297; and Phys. Rev. Lett. 65 (1990) 1301.
- [5] M. Koshiha, Proc. Workshop on Grand Unified Theories and Cosmology, KEK-84-12 KEK, Japan (1983) 24; Y. Totsuka, Proc. 7th Workshop on Grand Unification/ICOBAN'86, Toyama, Japan (1986) 118.